

A new limit on local Lorentz invariance violation of gravity from solitary pulsars

Lijing Shao^{1,2}, R. Nicolas Caballero¹, Michael Kramer^{1,3},
Norbert Wex¹, David J. Champion¹, Axel Jessner¹

¹ Max-Planck-Institut für Radioastronomie, Auf dem Hügel 69, D-53121 Bonn, Germany

² School of Physics, Peking University, Beijing 100871, China

³ Jodrell Bank Centre for Astrophysics, School of Physics and Astronomy, The University of Manchester, M13 9PL, UK

E-mail: lshao@pku.edu.cn (LS)

Abstract.

Gravitational preferred frame effects are generally predicted by alternative theories that exhibit an isotropic violation of local Lorentz invariance of gravity. They are described by three parameters in the parametrized post-Newtonian formalism. One of their strong-field generalizations, $\hat{\alpha}_2$, induces a precession of a pulsar's spin around its movement direction with respect to the preferred frame. We constrain $\hat{\alpha}_2$ by using the non-detection of such a precession using the characteristics of the pulse profile. In our analysis we use a large number of observations from the 100-m Effelsberg radio telescope, which cover a time span of approximately 15 years. By combining data from two solitary millisecond pulsars, PSRs B1937+21 and J1744–1134, we get a limit of $|\hat{\alpha}_2| < 1.6 \times 10^{-9}$ at 95% confidence level, which is more than two orders of magnitude better than its best weak-field counterpart from the Solar system.

PACS numbers: 04.80.Cc, 11.30.Cp, 97.60.Gb

1. Introduction

There are many models and test frameworks involving Lorentz violation in the gravitational sector, such as the vector-tensor theory in [68], TeVeS gravity [7, 52], Einstein-Æther theory [32], Hořava-Lifshitz gravity [30, 9], and the standard model extension (SME) of gravity [36, 6]. A preferred frame, possibly associated with the distribution of matter in the universe, may result, if the Lorentz violation is isotropic in a specific frame.

The existence of a preferred frame would induce various preferred frame effects (PFEs) that can be probed through different physical observables. In the parametrized post-Newtonian (PPN) formalism [68, 66], PFEs are characterized by three parameters, α_1 , α_2 and α_3 . In Einstein's general relativity (GR), $\alpha_1 = \alpha_2 = \alpha_3 = 0$. Their strong-field generalizations are denoted as $\hat{\alpha}_1$, $\hat{\alpha}_2$, and $\hat{\alpha}_3$, and again in GR, $\hat{\alpha}_1 = \hat{\alpha}_2 = \hat{\alpha}_3 = 0$. Nevertheless, one can have non-zero values of these parameters in alternative gravity theories [66, 67].

Observational implications of PFEs have been studied by several authors using different methods, α_i (as well as $\hat{\alpha}_i$; $i = 1, 2, 3$) are constrained to high precision from geophysics, Solar system, and pulsar timing experiments [48, 12, 58, 65, 54]. We briefly present the best limits of α_i (or $\hat{\alpha}_i$) below.

- Currently, the best limit on $\hat{\alpha}_1$ comes from the orbital dynamics of the binary pulsar PSR J1738+0333 [22], which gives a robust limit [54],

$$\hat{\alpha}_1 = -0.4^{+3.7}_{-3.1} \times 10^{-5}, \quad (95\% \text{ CL}). \quad (1)$$

- The best limit on α_2 comes from the alignment of the Sun's spin with the orbital angular momentum of the Solar system [47] (note, $\alpha_2^{\text{Nordtvedt}} = \frac{1}{2}\alpha_2$), which gives

$$|\alpha_2| < 2.4 \times 10^{-7}. \quad (2)$$

- The best limit on $\hat{\alpha}_3$ comes from the orbital dynamics of the statistical combination of a set of binary pulsars [58], which gives a probabilistic limit,

$$|\hat{\alpha}_3| < 4.0 \times 10^{-20}, \quad (95\% \text{ CL}). \quad (3)$$

As shown above, except for α_2 , pulsar timing observations have provided better limits than those from Solar system experiments. Here, however, one has to keep in mind, that pulsars are also sensitive to strong-field deviations, which do not occur in the weak-field regime of the Solar system. We note that, in general the preferred frame is not specified. The most natural option from a cosmological perspective is the frame where the cosmic microwave background (CMB) radiation is isotropic. The results discussed in this paper correspond to such a frame, however, see e.g. [65, 56, 54] for other preferred frames.

Since the first pulsar discovery in 1967 [26] more than two thousand pulsars have been discovered and studied with radio, X-ray and γ -ray observations [42]. These celestial objects are intriguing in multiple aspects, e.g., some of them show a long-term rotational stability similar to the stability of atomic clocks [29], their high interior density exceeds that of nuclear matter, and their high magnetic field is comparable to

or even exceeds the quantum critical value (see references in [40]). In particular, one of the most important contributions of pulsars is their unique rôle in tests of gravity theories, especially in the investigation of strong-field deviations from GR. To highlight some great achievements: i) the Hulse-Taylor pulsar provided the first evidence for the existence of gravitational waves [60, 61]; ii) the double pulsar provided the most accurate tests of GR in the strong-field regime, up to a precision of 0.05% [39]; iii) pulsar white dwarf systems provided the most stringent tests on the scalar-tensor theories [22, 1]. In this paper, we report a new limit on the (strong-field) PPN parameter $\hat{\alpha}_2$ from solitary millisecond pulsars (MSPs), which surpasses its current best weak-field counterpart from the Solar system [47] by more than two orders of magnitude.

The paper is organized as follows. In the next section, we introduce the α_2 (and $\hat{\alpha}_2$) parameter and its effect on the spin vector of solitary pulsars, which lays the principle of the test. In section 3, we present our two solitary pulsars, PSRs B1937+21 and J1744–1134, and the analysis of a large number of observations spanning about 15 years that were obtained from the 100-m Effelsberg radio telescope. Then in section 4, by using the non-detection of profile variation, we set a greatly improved constraint of $|\hat{\alpha}_2| < 1.6 \times 10^{-9}$ at 95% confidence level (CL). Section 5 discusses the relevance of our new limit, and briefly summarizes the paper. Throughout the paper, we use boldface letters to represent vectors, and put “hat” onto them to indicate their corresponding unit vectors. Strong-field generalizations of PPN parameters are distinguished explicitly by adding a “hat” onto their corresponding weak-field counterparts.

2. Preferred frame effects and $\hat{\alpha}_2$ -induced spin precession

Let us first summarize some key theoretical ingredients for the α_2 test. The α_2 -related many-body post-Newtonian Lagrangian term reads [47, 12],

$$L_{\alpha_2} = \frac{\alpha_2}{4} \sum_{i \neq j} \frac{Gm_i m_j}{c^2 r_{ij}} [(\mathbf{v}_i^0 \cdot \mathbf{v}_j^0) - (\hat{\mathbf{n}}_{ij} \cdot \mathbf{v}_i^0)(\hat{\mathbf{n}}_{ij} \cdot \mathbf{v}_j^0)] , \quad (4)$$

where \mathbf{v}_i^0 is the velocity of body i with respect to the preferred frame, r_{ij} is the coordinate separation of objects i and j , and $\hat{\mathbf{n}}_{ij} \equiv (\mathbf{r}_i - \mathbf{r}_j)/r_{ij}$. The velocity of the center-of-mass of the many-body system with respect to the preferred frame we denote by \mathbf{w} . Nordtvedt showed that, as a result of (4), the spin axis of a massive body precesses around \mathbf{w} . The precession has an angular velocity [47],

$$\Omega^{\text{prec}} = -\frac{\alpha_2}{2} \left(\frac{2\pi}{P} \right) \left(\frac{w}{c} \right)^2 \cos \psi , \quad (5)$$

where P is the spin period of the body’s rotation, ψ is the angle between \mathbf{w} and the spin direction $\hat{\mathbf{s}}$ (see figure 1 for angles and an illustration of the precession), and $w \equiv |\mathbf{w}|$. A similar consequence was also found in the orbital dynamics of a binary system (see (24) in [54]), where a (strong-field) $\hat{\alpha}_2$ induces a precession of the orbital angular momentum around \mathbf{w} for a small-eccentricity binary.

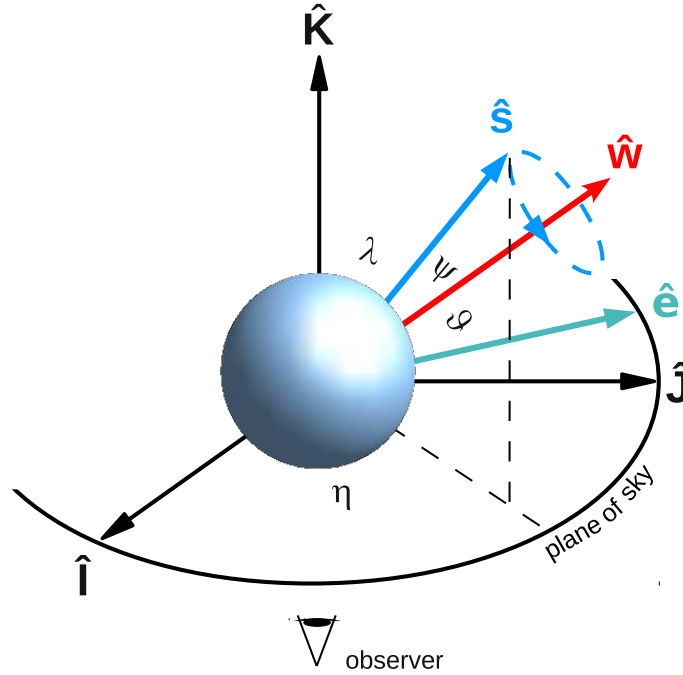


Figure 1. Angle notations and the $\hat{\alpha}_2$ -induced precession of the pulsar spin axis \hat{s} around \hat{w} , the movement direction of pulsar with respect to the preferred frame (see text). The coordinate system $(\hat{I}, \hat{J}, \hat{K})$ is defined with \hat{I} pointing to east, \hat{J} pointing to the north celestial pole, and \hat{K} pointing along the line of sight. The unit vector $\hat{e} \equiv \hat{K} \times \hat{s} / |\hat{K} \times \hat{s}|$ is in the sky plane.

As mentioned before, Nordtvedt [47] used the current alignment of the Sun’s spin with the orbital angular momentum of the Solar system, to limit such a precession. His limit (2) has remained the best limit of α_2 for more than a quarter of a century. The crucial assumption inherent is that the Sun’s spin *was* aligned with the Solar system angular momentum five billion years ago when the Sun was born. A weaker but more robust limit on α_2 comes from a long-term project called lunar laser ranging (LLR), which gives [45]

$$\alpha_2 = (1.8 \pm 5.0) \times 10^{-5}, \quad (95\% \text{ CL}), \quad (6)$$

from an analysis of 35 years of data. It is two orders of magnitude weaker than that of (2). The best limit in the strong field is from pulsar timing experiments on pulsar binaries PSRs J1012+5307 and J1738+0333 [54],

$$|\hat{\alpha}_2| < 1.8 \times 10^{-4}, \quad (95\% \text{ CL}). \quad (7)$$

The remarkable limit (2) obtained by Nordtvedt [47] benefited enormously from a long baseline of time of approximately five billion years. However, as we can see from (5), one can also take advantage of the short spin period of MSPs to achieve a tight constraint. This method was originally suggested in [47] shortly after the discovery of the first millisecond pulsar. We present the first detailed analysis in this direction.

With a non-vanishing $\hat{\alpha}_2$, a spinning pulsar would precess around its “absolute” velocity, \mathbf{w} , with an angular velocity (5). As a result of the precession, the angle, λ , between the pulsar spin axis and our line of sight changes with time (see figure 1), so that different portions of the pulsar emission beam are observed at different epochs. Consequently, one expects to detect characteristic changes in the measured pulse profile as a function of time. For solitary pulsars, from pure geometrical consideration we have (see also (2) in [4]),

$$\frac{d\lambda}{dt} = \Omega^{\text{prec}} \hat{\mathbf{w}} \cdot \left(\frac{\hat{\mathbf{K}} \times \hat{\mathbf{s}}}{|\hat{\mathbf{K}} \times \hat{\mathbf{s}}|} \right) \equiv \Omega^{\text{prec}} \cos \vartheta, \quad (8)$$

where ϑ is the angle between $\hat{\mathbf{w}} \equiv \mathbf{w}/w$ and $\hat{\mathbf{e}} \equiv \hat{\mathbf{K}} \times \hat{\mathbf{s}}/|\hat{\mathbf{K}} \times \hat{\mathbf{s}}|$. The unit vector, $\hat{\mathbf{e}}$, gives the line of nodes associated with the intersection of the sky plane and the equatorial plane of the pulsar (see figure 1).

Current observational technologies are already sensitive enough to detect such a change, if it exists. Indeed, similar changes in pulsar profiles have been observed before, albeit under the influence of geodetic precession, e.g. for, PSR B1913+16, PSR B1534+21, PSR J1141–6545, and PSR J0737–3039B [64, 37, 57, 44, 49]. Geodetic precession occurs in binary pulsars due to the curvature of spacetime near gravitating bodies, where the proper reference frame of a freely falling object suffers a precession with respect to a distant observer. The caused pulse profile changes manifested themselves in various forms [18], such as changes in the amplitude ratio or separation of two pulse components [64, 37], the shape of the characteristic swing of the linear polarization [57], or the absolute value of the position angle [44].

For our purpose, to avoid complications due to spin-orbit coupling, we choose solitary pulsars to limit $\hat{\alpha}_2$. In our solitary pulsars below, if there exists an $\hat{\alpha}_2$ -induced precession, we are also expected to observe one or several of the above mentioned changes in the pulse profile. On the other hand, if we do not see any changes in the observations, we can constrain $\hat{\alpha}_2$. As an example of such a non-detection, in figure 2 we plot two pulse profiles of PSR B1937+21 obtained at different epochs. One was obtained on September 2, 1997, while the other was obtained on June 6, 2009. Details of the used observing system will be given given in Section 3. Instrumental effects are responsible for the “dips” around the pulse. We have not removed these effects since we only use data from one backend and the dips remain unchanged in time and do not introduce any temporal variation in the profiles. We can immediately see from figure 2 that within noise, there is no visible change in the pulse profile for this pulsar over more than ten years. The two profiles are chosen solely based on a large time separation and a low level of noise, so that no bias is introduced. A similar overlap of two pulse profiles for the other pulsar in our test, PSR J1744–1134, is shown in figure 3. The profiles were obtained on April 29, 1998 and September 8, 2008. There exists no visible difference within noise level. These two solitary pulsars are selected from the known population of millisecond pulsars, based on their figure of merit for the $\hat{\alpha}_2$ test. The figure of merit is roughly $P^{-1}T_{\text{obs}}^{3/2}$ where T_{obs} is the observational time span. We also require the pulsars

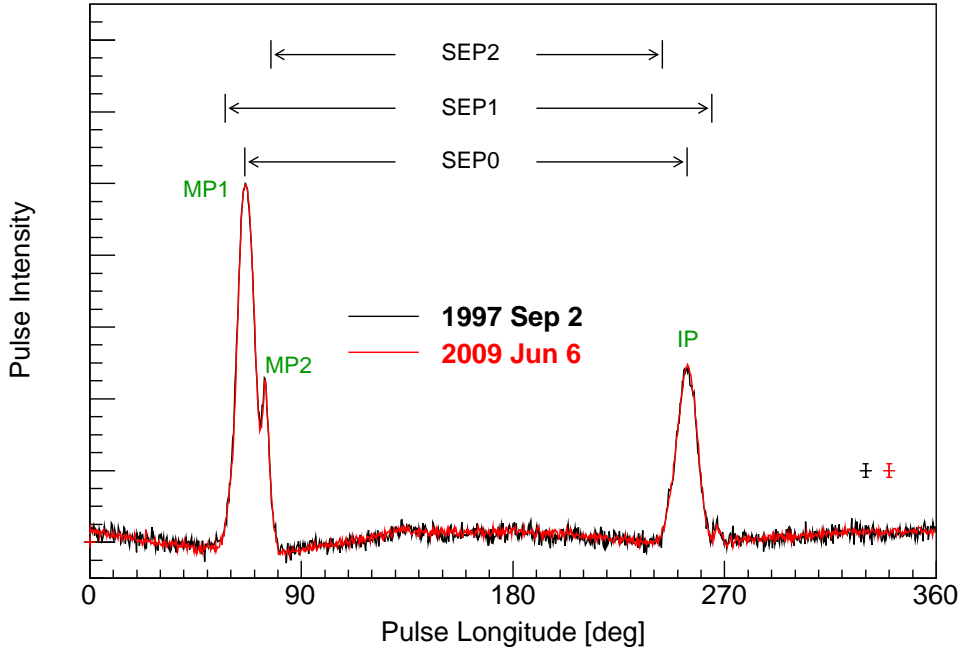


Figure 2. Comparison of two pulse profiles of PSR B1937+21 obtained at two different epochs — the black one was obtained on September 2, 1997, while the red one was obtained on June 6, 2009. The main peak is aligned and scaled to have the same intensity. Uncertainties in pulse profiles are illustrated at the right bottom corner. Notations used in figure 4 include: the first component of the main-pulse (MP1), the second component of the main-pulse (MP2), the interpulse (IP), the separation between MP1 and IP (SEP0), the separation between leading MP1 and trailing IP (SEP1), and the separation between trailing MP2 and leading IP (SEP2).

to have proper motion measurements from pulsar timing and geometry information from the combination of radio and γ -ray observations. The reason for the figure of merit and these requirements will become clear later.

To achieve a quantitative constraint, we need to relate the change in λ with that of a profile. One can confidently consider the pulse profile as a cross-sectional cut through the pulsar’s emission beam [40]. To quantify the (non-)change of pulsar geometry from a pulse profile, we should introduce a basic emission model. We use the simplest geometrical cone model [23], which only assumes that radio beam is centred on the magnetic axis, causing the “lighthouse” effect of a pulsar as it rotates around the spin axis. This approximation avoids most of the model dependent aspects of pulsar emission, and sufficiently reproduces the basic features of the two solitary pulsars we are using here. We note in passing that the limit on the pulsar spin precession does not depend on this assumption significantly, as shown in the geodetic precession analysis for PSR J0737–3039A [43]. The latter is also a non-detection case, where authors showed that a non-zero ellipticity for the radiation beam gives no significantly improved fits to

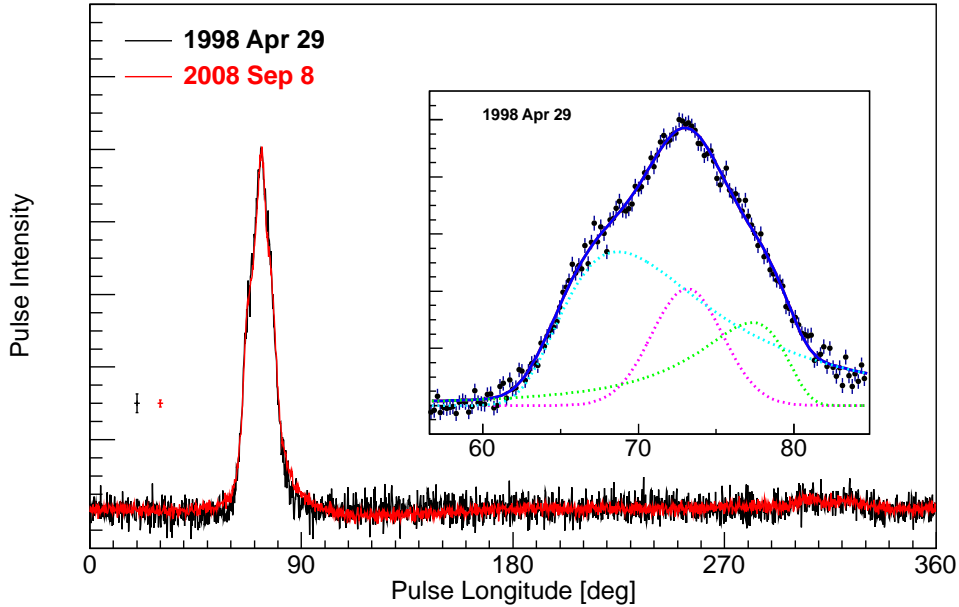


Figure 3. A comparison of two pulse profiles of PSR J1744–1134 obtained during two different epochs — the black one was obtained on April 29, 1998, while the red one was obtained on September 8, 2008. The peak is aligned and scaled to have the same intensity. Uncertainties in pulse profiles are illustrated at the left bottom corner. Inset shows the zoom-in of the main pulse (corresponding to the black profile in the main figure), and it also shows our analytical fitting to the pulse and the corresponding three components (see text).

the data, and a circular beam describes the data equally [43].

From the cone model, it was shown from geometry [23, 40],

$$\sin^2\left(\frac{W}{4}\right) = \frac{\sin^2(\rho/2) - \sin^2(\beta/2)}{\sin(\alpha + \beta) \sin \alpha}, \quad (9)$$

where W is the width of the pulse, α is the angle between \hat{s} and the magnetic axis, $\beta \equiv 180^\circ - \lambda - \alpha$ is the impact angle, and ρ is the semi-angle of the opening radiating region (for details, see [40] and references therein).

Adopting a plausible assumption that the radiation property (α and ρ) has no change during the observational span ~ 15 years [40], i.e. $d\alpha/dt = d\rho/dt = 0$, we can relate the change in λ with the change in the pulse width (see also (4) in [11]),

$$\frac{d\lambda}{dt} = \frac{1}{2} \frac{\sin(W/2)}{\cot \lambda \cos(W/2) + \cot \alpha} \frac{dW}{dt} \equiv \mathcal{A} \frac{dW}{dt}, \quad (10)$$

where $\mathcal{A} \equiv \sin(W/2)/[2 \cot \lambda \cos(W/2) + 2 \cot \alpha]$. Hereafter we use the width at 50% intensity level, W_{50} , as a proxy of W .[‡] Now we can quantify the (non-)change of the pulsar orientation with respect to the Earth through the (non-)change in the pulse

[‡] Other choices, like the width at a 10%-level do not change the result in the following significantly.

width. In the next section, detailed constraints on the (non-)change of pulse width are derived, which are used to put a limit on $\hat{\alpha}_2$ in section 4.

3. Observations and pulse profile analysis

In this section, we present our observations of two solitary pulsars with the 100-m Effelsberg telescope and our detailed analysis of pulse profiles.

All data were obtained with the 100-m Effelsberg radio telescope, operated by the Max-Planck-Institut für Radioastronomie, Bonn, Germany. The observations are part of the pulsar timing program (see e.g. [20, 25]). In order to examine the profile stability over time, it is important to use data obtained with as few changes in the observing system as possible. The major components of the system are the telescope, the receiver (frontend) and the data processor (backend).

The observations span from September 1997 for PSR B1937+21 and January 1997 for PSR J1744–1134, to the present. Receiver systems operating at a frequency around 1400 MHz were used, being sensitive to two orthogonally left-hand and right-hand circularly polarised signals. The frequency of the signals was mixed to baseband and fed into a data acquisition system known as the Effelsberg-Berkeley Pulsar Processor (EBPP) [2]. The EBPP is a coherent dedispersion backend which means that it completely removes the signal dispersion effect of the interstellar medium (ISM) caused by free electrons along the line of sight. If left uncorrected this causes an apparent broadening of the pulse. The time resolution of our equipment was $1.4 \mu\text{s}$ for PSR B1937+21 and $0.6 \mu\text{s}$ for PSR J1744–1134. In the backend the signal from the channels is directed to the dedisperser boards where online coherent dedispersion takes place according to the recorded dispersion measure (DM)[§]. The output signals are folded using the topocentric pulse period (i.e. individual pulses are phase-aligned and added), and are later integrated in phase. The EBPP is the longest-running coherent dedispersion backend dedicated to high precision pulsar timing, making its database uniquely suited this work. The total bandwidth of the EBPP is dependent on the source’s dispersion smearing at the observing frequency and has a maximum value of 112 MHz. The observational bandwidth for PSR B1937+21 is 44 MHz, while for PSR J1744–1134, all data have 112 MHz of bandwidth apart from the first two observations in January 1997 which have 56 MHz of bandwidth. The frontend of the telescope changed once in July 2009, resulting in a change of the central frequency from 1410 MHz to 1360 MHz. Frequency evolution of the profile is very small for MSPs but we quantified the change in profiles in section 3.1.

The data were reduced using the PSRCHIVE package [31]. Each profile we use is a ~ 30 minute integration. This is achieved by adding shorter integrations made with no more than one hour separation. Throughout the pulse profile fitting analysis discussed in the following, we use the off-pulse root-mean-square as the profile’s flux uncertainty.

[§] DM is defined as the integrated column density of free electrons in the ISM along the line of sight, $\text{DM} \equiv \int n_e dl$ [40].

Table 1. Relevant quantities of PSRs B1937+21 and J1744–1134 for the $\hat{\alpha}_2$ test. Most quantities are from pulsar timing [62], while the orientation and radiation quantities (α and ζ) were obtained from model fitting to radio and γ -ray lightcurves (PSR B1937+21 [24] and PSR J1744–1134 [34]). The Lutz–Kelker bias in the timing parallax was corrected [63]. The scattering timescales were calculated according to an empirical relationship in [8], and listed for 1410 MHz/1360 MHz. The pulse width and its time derivative are from this work. For PSR B1937+21, quantities for MP1 (left) and IP (right) are both tabulated. Parenthesized numbers represent the 1- σ uncertainty in the last digits quoted.

Pulsar	B1937+21	J1744–1134
Discovery (year)	1982 [3]	1997 [5]
Right Ascension, α (J2000)	19 ^h 39 ^m 38 ^s .561297(2)	17 ^h 44 ^m 29 ^s .403209(4)
Declination, δ (J2000)	+21°34′59″.12950(4)	−11°34′54″.6606(2)
Spin period, P (ms)	1.55780653910(3)	4.074545940854022(8)
Reference epoch for α , δ and P (MJD)	54219	53742
Proper motion in α , μ_α (mas yr ^{−1})	0.072(1)	18.804(8)
Proper motion in δ , μ_δ (mas yr ^{−1})	−0.415(2)	−9.40(3)
Parallax, π (mas)	0.14 ^{+0.05} _{−0.03}	2.4(1)
Dispersion measure, DM (cm ^{−3} pc)	71.0227(5)	3.1380(3)
Magnetic inclination, α (deg)	75 ⁺⁸ _{−6} 105 ⁺⁶ _{−8}	51 ⁺¹⁶ _{−19}
Observer angle, ζ (deg)	80(3)	85 ⁺³ _{−12}
Scattering timescale, τ_s (ns)	826/949	0.20/0.23
Time span of data used in this work (MJD)	50693–55725	50460–55962
Pulse width at 50% intensity, W_{50} (deg)	8.281(9) 10.245(17)	12.53(3)
Time derivative of W_{50} , dW_{50}/dt (10 ^{−3} deg yr ^{−1})	−3.2(34) 3.5(66)	1.3(72)
Jump between two frequencies, ΔW_{50} (deg)	0.12(3) 0.04(6)	–

3.1. PSR B1937+21

PSR B1937+21 (a.k.a PSR J1939+2134) was the first MSP discovered, with a spin period of 1.56 ms [3]. Because of its brightness and later as a target of pulsar timing array (PTA) projects [28, 20, 25], it has been observed frequently since its discovery. PSR B1937+21 shows a strong main-pulse (MP1) with a second weaker component (MP2) and a strong interpulse (IP), see figure 2 for illustrations. The main-pulse and interpulse are separated by $\sim 188^\circ$, hence they may be produced by two opposite magnetic poles sweeping over the Earth. Another possibility is that they are produced by a single magnetic pole with a wide opening angle and a hollow cone emission pattern.

In order to examine the profiles, we performed least-square fitting of parabolas to the peaks of the three components. The simplicity of the components’ shapes allows good fits with a simple and symmetric function, preserving linearity of the fitting

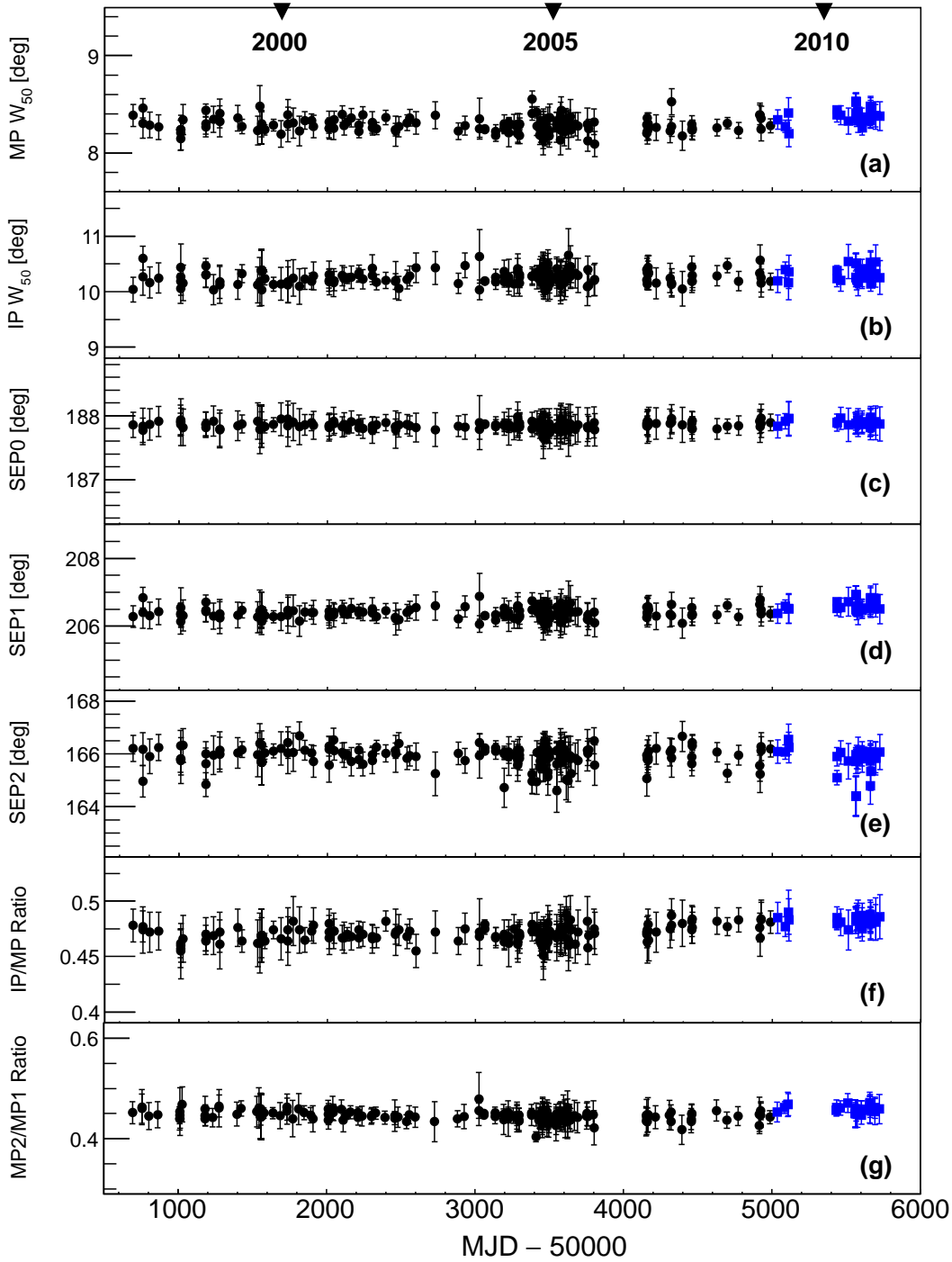


Figure 4. Pulse profile characteristics of PSR B1937+21, as a function of modified Julian date (MJD); see figure 2 for notations. The amplitude ratios in (f-g) are measured from peak to peak. Black circles are observations made at 1410 MHz, while blue squares are observations made at 1360 MHz. Years of observations are indicated at the top of the figure.

procedure. For each component we obtained the peak intensity and its corresponding longitude value as well as its W_{50} . We investigated the time stability of the pulse profile using five different measurements of widths and component separations (see figure 2 for definitions) and also two measurements of amplitude ratios of different components. The results from fitting are plotted in figure 4 as a function of time.

One can see that the seven quantities characterizing the pulse profile are very stable over the 15 years of observation. We also plotted twelve high signal to noise ratio (S/N) profiles in the left panel of figure 5. These profiles span almost uniformly the whole observing period from 1997 to 2011. In the right panel of figure 5, the difference between profiles is present after subtracting a reference profile. The highest S/N reference profiles are chosen for each frequency — one obtained on January 4, 1999 for 1410 MHz and one obtained on August 26, 2010 for 1360 MHz. We can see from the residuals that no evolution over time in the profile is visible.

Concerning the frequency dependence of W_{50} , in general normal pulsars|| show a systematic increase in pulse width when observed at lower frequencies [40], while MSPs in general show very little evolution of pulse width with frequency [38]. Nevertheless, for both normal pulsars and MSPs, profile evolution, in terms of peak intensities, width and phase, was observed. In figure 4, one can see that there is no large difference between two frequencies. However, in our accurate data, we found that a subtle change between two frequencies is needed. Therefore we fitted W_{50} 's of the main-pulse and the interpulse with the following formula,

$$W_{50}(t) = W_{50} + \frac{dW_{50}}{dt}t + \Delta W_{50} \Theta(t - t_0), \quad (11)$$

where ΔW_{50} is the ‘‘jump’’ of width between measurements made at 1360 MHz and 1410 MHz, $\Theta(t)$ is the Heaviside step function, and t_0 is the time when observations were shifted from 1410 MHz to 1360 MHz.

We simulated 10^6 sets of profile widths against time according to the measurements and uncertainties in figure 4(a), and then fitted simultaneously for three parameters in (11) for each set of profile widths. The fitted parameters were accumulated as histograms with 10^6 entries. We read out the fitting results and their uncertainties from the central values and the widths of these histograms respectively. They are tabulated in the last three rows in table 1, where uncertainties are rescaled by the square root of the reduced fitting χ^2 , χ_{red}^2 . The results show the need of a tiny jump $\Delta W_{50} \simeq 0.1^\circ$ (about one third of a bin in the EBPP profile data).

We investigated the possible origin of the jump by effects associated with ISM. For pulsars such as PSR B1937+21 with high DM, ΔW_{50} may reflect the scattering effects from the irregularities in the ISM, which usually produce a one-sided exponential tail for pulsar profiles [40]. The scattering timescales for the two frequencies are listed in table 1, and are based on an empirical dependence on DM and frequency [8]. The broadening in the pulse width from the intrinsic profile to profile at 1410 MHz is less

|| Normal pulsar usually means a non-recycled pulsar with a spin period P larger than 30 ms, and a spindown rate $\dot{P} \sim 10^{-18}$ to 10^{-15} ss^{-1} ; see references in [40] for details.

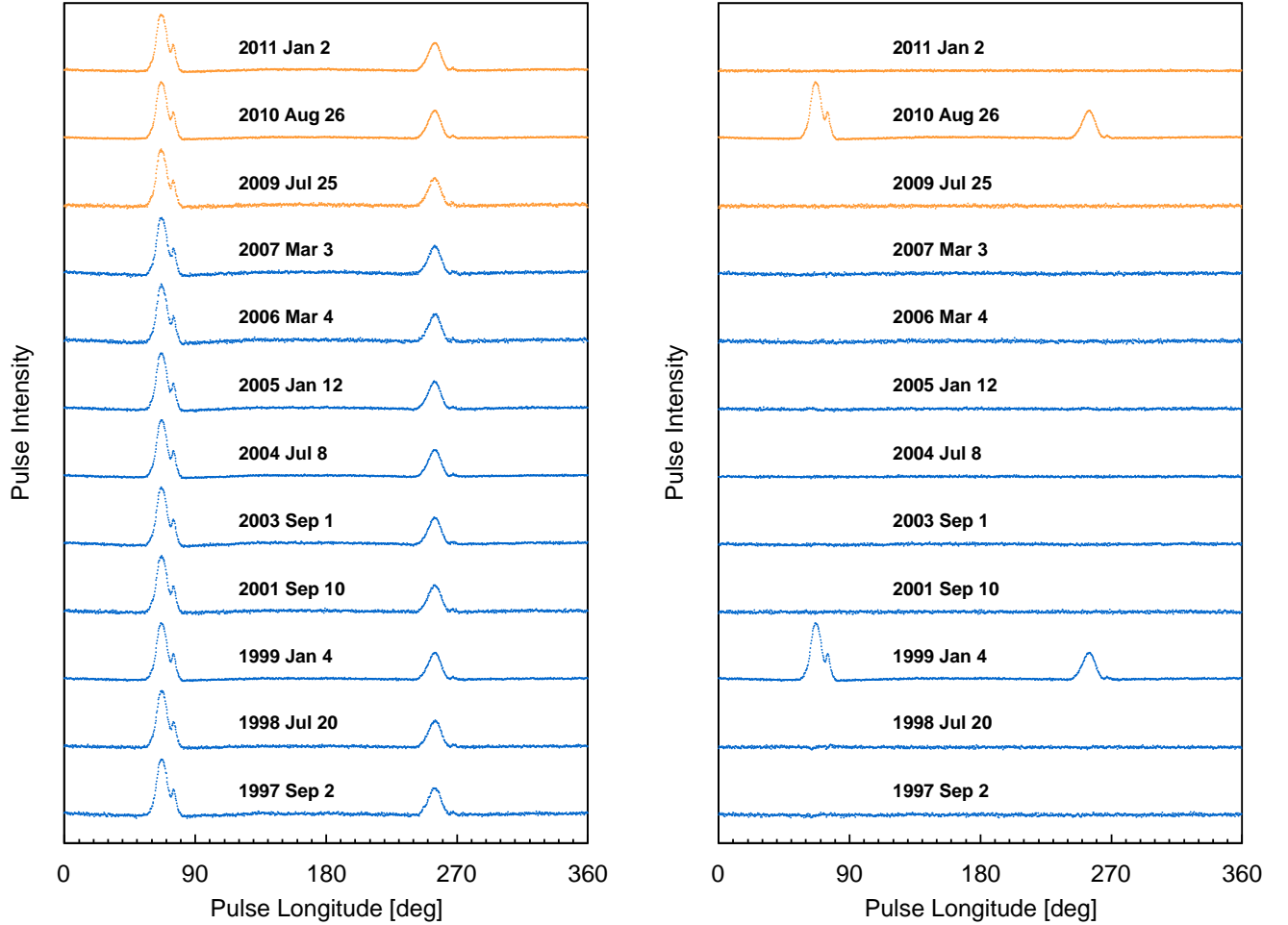


Figure 5. Integrated pulse profiles and difference profile residuals for PSR B1937+21, obtained from the 100-m Effelsberg radio telescope. Orange/Blue profiles are obtained from observations made with the central frequency 1360 MHz/1410 MHz. *Left:* Twelve high S/N, aligned and normalized pulse profiles that are labeled with dates of the observation epochs. *Right:* A reference profile is subtracted from each of the other profiles of the same observational frequency. The pulse profiles taken on January 4, 1999 and August 26, 2010 are used as reference profiles for two different frequencies; reference profiles are still plotted in the right panel.

than 0.02° for PSR B1937+21 from scattering, and the difference between 1410 MHz and 1360 MHz is roughly $(\Delta W_{50})^{\text{scattering}} \simeq 0.004^\circ$, hence negligible. The empirical relation in [8] is poorly constrained and may introduce overestimation or underestimation to an amount of several times, however, after taking the uncertainties into account, the effects from scattering are still too small to account for the ΔW_{50} we obtained from fitting. Another factor to consider is temporal DM variation. It is well known that the DM varies with time and various efforts were made to measure these variations systematically, see

e.g. [69]. If the DM at the observatory is not properly updated, then the dedispersion would be imperfect, leading to a broader pulse. We have calculated the width difference between the two frequency bands for a DM value that deviates as much as $0.05 \text{ cm}^{-3} \text{ pc}$ from the correct value (it would take decades without updating the DM value to get such a large deviation for PSR B1937+21 [51, 69]), and we found that the ΔW_{50} between the 1410 MHz and 1360 MHz bands are below a few times 0.001° . Therefore, the effects from DM variation are also negligible. In order to test for the possibility that ΔW_{50} is caused by profile evolution we made use of data taken at Effelsberg with **Asterix**, a new backend that has run in parallel with the EBPP since 2011. **Asterix** has a broader bandwidth of 200 MHz. The frequency range covers both frequency bands of the EBPP backend. We selected the **Asterix** frequency range accordingly to emulate the EBPP characteristics and found a jump $\Delta W_{50} \simeq 0.07^\circ \pm 0.03^\circ$ between two frequencies, which is consistent with the jump from the EBPP backend. Consequently, we conclude that ΔW_{50} reflects an evolution of the pulsar profile width with frequency¶.

The same Monte Carlo fitting analysis was also applied to the interpulse (figure 4(b)); see table 1 for the fitted results. We detected no changes in the pulse width against time for the interpulse as well.

For both the main-pulse and the interpulse, we find no evidence of changes in the pulse width over time. We also performed hypothesis test to test the necessity of a non-zero (dW_{50}/dt) for main-pulse and interpulse. Our null hypothesis is that, the inclusion of (dW_{50}/dt) does not provide a significantly better fit. F -tests give p -values of 0.22 and 0.31 for the null hypothesis of the main-pulse and interpulse respectively, which clearly show that the inclusion of a non-zero (dW_{50}/dt) does not provide a significantly better fit to the data⁺.

3.2. PSR J1744–1134

PSR J1744–1134 was discovered in 1997 through the Parkes 436 MHz survey of the southern sky [5]. It has a spin period of 4.07 ms, and later as a target in the PTA projects [28], it is being observed frequently. PSR J1744–1134 has a sharp pulse with a $W_{50} \sim 12.5^\circ$ at 1410 MHz, see figure 3. Because of a long observational span in time and continuous observations since its discovery, it is also a good laboratory to test the local Lorentz invariance of gravity.

We used 65 observations spanning about 15 years obtained with the 100-m Effelsberg radio telescope. In order to measure the pulse width accurately, we again try to describe the profile by an analytic function. The pulse profile of PSR J1744–1134 is different from that of PSR B1937+21, where we used fits of parabolas to parts of the

¶ See also figure 13 in [38] for the evolution of pulse profile of PSR B1937+21 with frequency. Note that in the relevant frequency bands, the dip between MP1 and MP2 gets deeper when frequency increases, consequently the width of MP1 gets narrower. This is also consistent with the ΔW_{50} measurement here.

⁺ The p -value from the test is the probability of obtaining a test statistic at least as extreme as the one that is actually observed, assuming that the null hypothesis is true [50]. In our cases, the test statistic is F statistic which follows an F distribution.

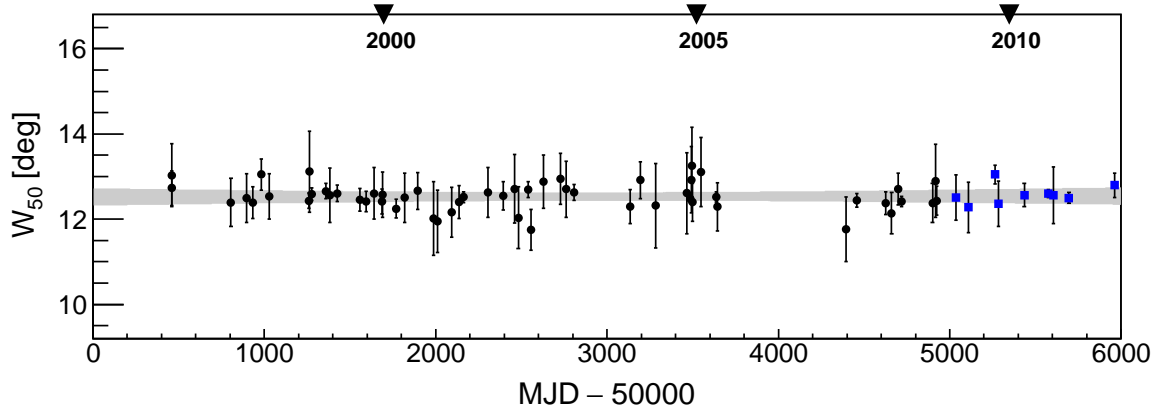


Figure 6. Pulse width at 50% intensity level of PSR J1744–1134, as a function of time. Black circles are observations made at 1410 MHz, while blue squares are observations made at 1360 MHz. Errors are rescaled by the square root of the fitting χ_{red}^2 . The gray region shows the $3\text{-}\sigma$ band of our linear fitting. The years of observations are indicated at the top of the figure.

pulse to determine the width. The same method cannot be applied here, and different functions need to be used. Despite the apparent simplicity of the pulse, a good fit to a high S/N pulse profile is not trivial, see e.g. figure 4 in [41] where seven Gaussian components were used for the whole profile at 1400 MHz observational frequency (five Gaussian components for the main-pulse). In this work we used three components to fit the main-pulse of PSR J1744–1134. These components have close centre values, so using three Gauss functions would often not give a stable fitting result, unless we a priori fix the means of them. Therefore we used three components with different shapes (one Gauss function and two Landau functions with opposite orientations) to break the degeneracy and achieve a stable fitting. A typical fitting is shown in the inset of figure 3. For each observation, we generated 10^4 realizations of the profile according to measurement and measurement uncertainty. Then for each profile, we fitted the three components analytically. W_{50} is obtained from the analytical sum of these components. Hence for one observation, we have a distribution of pulse width with ten thousand entries. A width with an uncertainty is drawn from this distribution. Finally the uncertainty is rescaled by the square root of the fitting χ_{red}^2 . The result is plotted in figure 6 as a function of time. No clear evolution over time is seen from the pulse width. Because of fewer observations and lower S/N of the profile data on average of PSR J1744–1134, the uncertainties in W_{50} are in general larger than that of PSR B1937+21.

Twelve high S/N profiles of PSR J1744–1134 are present in figure 7 in a similar way as PSR B1937+21 in figure 5. For this pulsar, we see no evolution between two frequencies. We performed the same check as with PSR B1937+21 using *Asterix* data of PSR J1744–1134, and no evolution of the profile width between two frequencies is found. Hence, we only used one reference profile for subtraction. From the residuals in

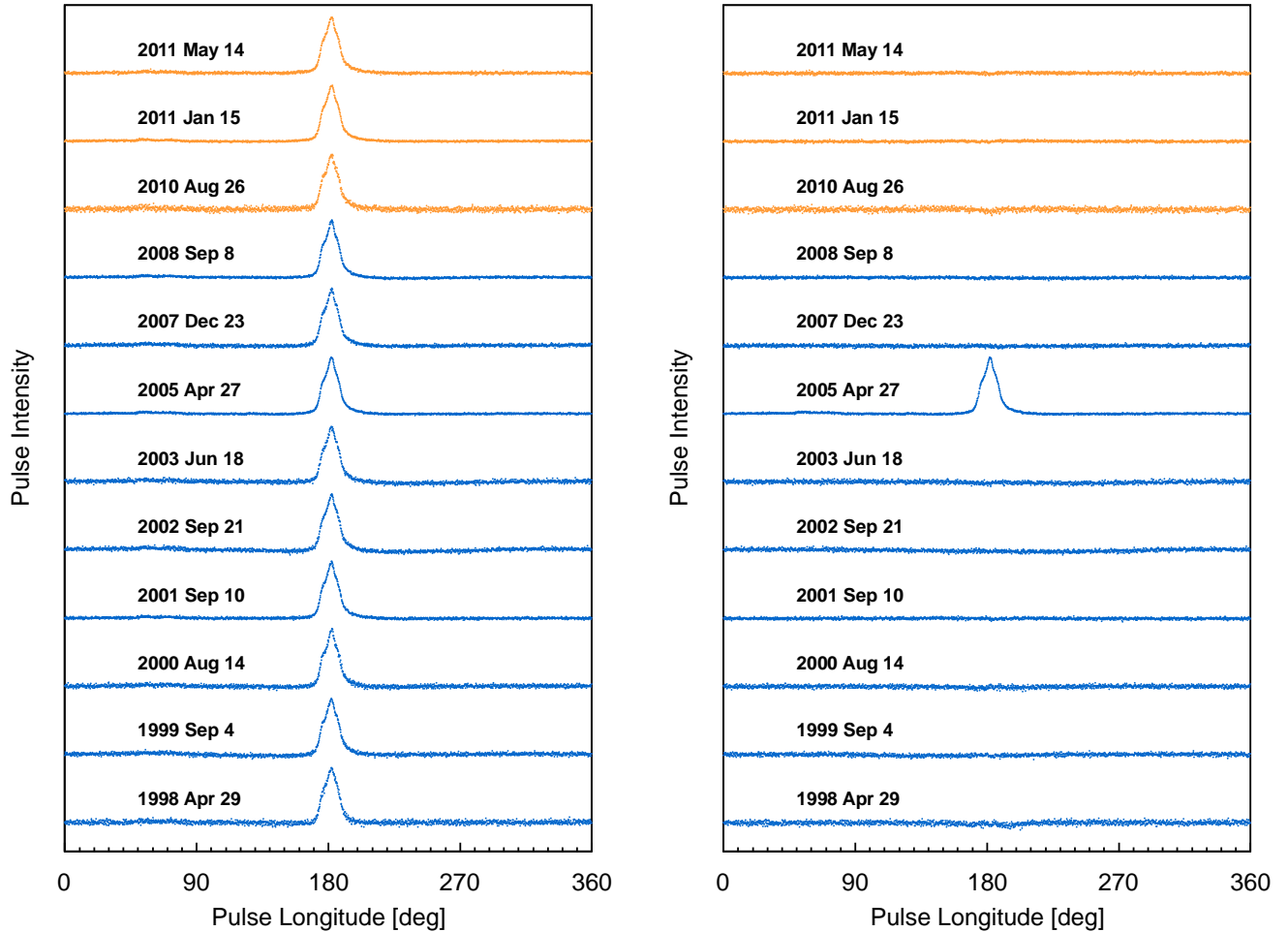


Figure 7. Same as figure 5, for PSR J1744–1134. For the right panel, the pulse profile taken on April 27, 2005 is used as the reference profile for subtraction.

the right panel, one finds no change in pulse profile over ~ 15 years.

The same Monte Carlo and fitting analysis applied to PSR B1937+21 (see section 3.1) was implemented for PSR J1744–1134. For this pulsar, we used the linear function (11) without the need of a jump in pulse width. The fitting results from 10^6 simulations are tabulated in table 1. As was the case for PSR B1937+21, the measurement of (dW_{50}/dt) shows no significant change in W_{50} over time for PSR J1744–1134. F -test [50] gives a p -value of 0.44 for the necessity of a non-zero (dW_{50}/dt) .

4. A new $\hat{\alpha}_2$ limit from solitary pulsars

From the pulse-profile analysis of PSRs B1937+21 and J1744–1134, tight limits on the change of pulse width have been set (see table 1). We have also examined the profiles of PSRs B1937+21 and J1744–1134 from early literature and no change was found. Because of low quantity of early data and the use of different backends, they have not been included in the calculations.

By combining (5), (8) and (10), we have

$$\hat{\alpha}_2 = -2 \mathcal{A} \left[\frac{2\pi}{P} \left(\frac{w}{c} \right)^2 \cos \psi \cos \vartheta \right]^{-1} \frac{dW}{dt}. \quad (12)$$

The limits on width changes for PSRs B1937+21 and J1744–1134 were given in section 3. The others will be discussed in the following.

\mathcal{A} is defined in (10) and includes information of the pulse profile, the spin orientation and the emission property. Pulse width is obtained from profile analysis, while λ (or equivalently the observer angle $\zeta \equiv 180^\circ - \lambda$) and α can be obtained from lightcurve analysis by combining radio and γ -ray observations. For both PSRs B1937+21 and J1744–1134, γ -ray observations from Fermi Large Area Telescope (LAT) are available [24, 34]. The results from modeling of the radio and γ -ray emission profiles are quoted in table 1 for PSR B1937+21 [24] and PSR J1744–1134 [34].

To obtain the quantities inside the square brackets of (12), besides the well measured spin period (see table 1), we need to know the pulsar’s velocity with respect to the preferred frame, and the pulsar’s spin orientation with respect to it.

First, a preferred frame must be specified. The most natural frame is the one where the CMB radiation is isotropic. The CMB frame is used as the preferred frame in most literature (see however [65, 56, 54] for other local frames), and the constraints of α_i (and $\hat{\alpha}_i$) quoted in section 2 all refer to this frame. We will also use the CMB frame as the preferred frame in the following calculations. This choice basically assumes that the preferred frame is determined by the global distribution of matter in the Universe, and that the fields of the gravitational interaction, which cause the PFEs, are long range, at least comparable to the Hubble radius. The generalization to other frames is straightforward.

From Wilkinson Microwave Anisotropy Probe (WMAP) observations, our Solar system barycenter (SSB) has a peculiar velocity with respect to the CMB frame, $|\mathbf{w}_{\text{SSB}}| = 369.0 \pm 0.9 \text{ km s}^{-1}$, in the direction of Galactic longitude and latitude $(l, b) = (263.99^\circ \pm 0.14^\circ, 48.26^\circ \pm 0.03^\circ)$ [27, 33]. The pulsar velocity with respect to the CMB frame is simply $\mathbf{w} = \mathbf{v}_{\text{PSR-SSB}} + \mathbf{w}_{\text{SSB}}$, where $\mathbf{v}_{\text{PSR-SSB}}$ is the 3D motion of the pulsar with respect to SSB. The 2D projected movement on the sky plane can be obtained from proper motion and parallax measurements from timing experiments [62] (see table 1). The parallax of PSR B1937+21 is not well measured, so the distance estimated from it is not accurate. Different Galactic electron density models [59, 10, 53] infer a distance in the range of 3.6–4.8 kpc (D. Schnitzeler, private communication), coarsely consistent with the distance derived from the parallax. Fortunately, because of

the small angular proper motion of PSR B1937+21 ($\mu_T \equiv \sqrt{\mu_\alpha^2 + \mu_\delta^2} \simeq 0.42 \text{ mas yr}^{-1}$; see table 1), the error of the 2D velocity is less than 10 km s^{-1} even if we underestimate or overestimate the distance by a few kpc. The radial velocity $v_r \equiv \hat{\mathbf{K}} \cdot \mathbf{v}_{\text{PSR-SSB}}$ of solitary pulsars in general is not measurable from pulsar timing experiments. However, we can see in the following that it only has slight effects on the test. The radial velocity enters in (12) through \mathbf{w} , in the form of $(\mathbf{w} \cdot \hat{\mathbf{s}})^*$. From Fermi LAT γ -ray observations, we can see that the spins of PSRs B1937+21 and J1744–1134 both lie close to the sky plane ($\zeta \sim 80^\circ$; see table 1), so the unknown radial velocity only has a marginal effect in $(\mathbf{w} \cdot \hat{\mathbf{s}})$. By assuming that the solitary pulsars are gravitationally bound in the Galaxy [35], we find that the reasonable ranges of the radial velocities are $-600 \text{ km s}^{-1} \lesssim v_r \lesssim 200 \text{ km s}^{-1}$ for PSR B1937+21 and $-400 \text{ km s}^{-1} \lesssim v_r \lesssim 250 \text{ km s}^{-1}$ for PSR J1744–1134, respectively. We use these ranges to test the dependence of our $\hat{\alpha}_2$ limits on the radial velocity later on, and the results only show a weak dependence that alters the limits by $\sim 15\%$ at most. Even if we assume some unphysical radial velocity $|v_r| \gtrsim 1000 \text{ km s}^{-1}$, the limits are altered by $\sim 40\%$ at most. In the case of extremely large radial velocities $|v_r| \gtrsim 1500 \text{ km s}^{-1}$, the $\hat{\alpha}_2$ limits get better with increasing $|v_r|$.

For the pulsar spin orientation, as mentioned before, ζ can be inferred from the combination of radio and Fermi LAT observations. The remaining unknown is the azimuthal angle η of the pulsar spin $\hat{\mathbf{s}}$ around the line of sight (see figure 1), which is not an observable from pulsar observations for PSRs B1937+21 and J1744–1134 and will be treated as a random variable.

We set up Monte Carlo simulations to account for measurement errors and the unknown η and the unknown radial velocity. In our simulation, we assume that the radial velocity follows a Gaussian distribution with a zero mean and a 100 km s^{-1} spread, and η is treated as a random variable uniformly distributed in $(0^\circ, 360^\circ)$, in the same way as that of [17, 12]. As mentioned before, we also set up various Monte Carlo simulations for different radial velocities, where only a weak dependence on the choice of the radial velocity is found, at most altering our results by $\sim 15\%$ under the assumption that the solitary pulsars are bound in the gravitational potential of the Galaxy. Because of the unknown η , our final result is a probabilistic constraint, the same as the strong equivalence principle test in [17] and the $\hat{\alpha}_1$ test in [12]. It is the main limitation of these tests (see [54] for a robust $\hat{\alpha}_1$ test where such a probabilistic assumption was overcome). Through 10^8 simulations, we got the probability density functions (PDFs) of $\hat{\alpha}_2$ from PSRs B1937+21 and J1744–1134 according to (12). They are plotted in figure 8 as a blue dashed histogram and a red dotted histogram, respectively. From these PDFs, we obtain

$$\text{PSR B1937+21: } |\hat{\alpha}_2| < 2.5 \times 10^{-8}, \quad (95\% \text{ CL}), \quad (13)$$

$$\text{PSR J1744–1134: } |\hat{\alpha}_2| < 1.5 \times 10^{-8}, \quad (95\% \text{ CL}). \quad (14)$$

They are already much better than the limit (2) from the Solar system. For these limits, PSR B1937+21 benefits from a smaller spin period and a tighter constraint on

* It has no contribution to $(\mathbf{w} \cdot \hat{\mathbf{e}})$ because by definition $\hat{\mathbf{e}}$ is in the sky plane.

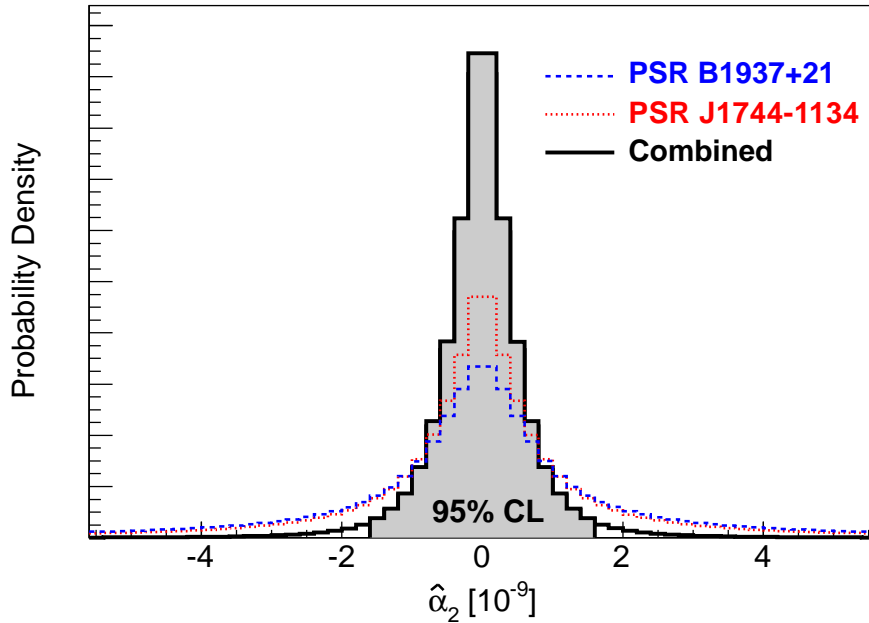


Figure 8. Probability density functions of $\hat{\alpha}_2$ from PSR B1937+21 (blue dashed histogram), PSR J1744–1134 (red dotted histogram), and their combination (black solid histogram). At 95% confidence level, $|\hat{\alpha}_2|$ is constrained to be less than 1.6×10^{-9} from the combined probability distribution.

dW_{50}/dt (see table 1), however PSR J1744–1134 benefits from a more favorable emission geometry (a smaller \mathcal{A}). In total, PSR J1744–1134 gives a slightly better limit than PSR B1937+21. The analysis for PSR B1937+21 is based on the main-pulse (MP1 in figure 2). Likewise, one could use the interpulse (IP in figure 2) to constrain a precession of PSR B1937+21, which leads to a similar, even slightly more constraining limit because of a smaller \mathcal{A} . We therefore stay with the more conservative value derived from the main-pulse. Similarly, even though the results at γ -ray frequencies convincingly rule out such an interpretation, one may consider the main- and interpulse as the result of a single very wide cone. In that case, the interpretation of the change in width as described in (10) will need to be recasted in terms of the IP-MP separation (SEPO in figures 2 and 4). Such an interpretation would give similar limits.

We can immediately see that the above two numbers are located far outside the $\hat{\alpha}_2$ range plotted in figure 8. This is due to the fact that these PDFs have very long tails (compared with the normal distribution). The reason for the long tail was analyzed explicitly in [54] for a similar $\hat{\alpha}_2$ test from binary dynamics. They are due to unfavorable geometrical configurations where $\cos \psi \simeq 0$ and/or $\cos \vartheta \simeq 0$. From (12), we can see that $\hat{\alpha}_2$ is unconstrained at these configurations. Fortunately, as in [54] one can take advantage of the probabilistic consideration by using more than one system to suppress the long tails. The probability that *both* pulsars are at their unfavorable orientation is small. For this reason we use more than one solitary pulsar. By assuming that

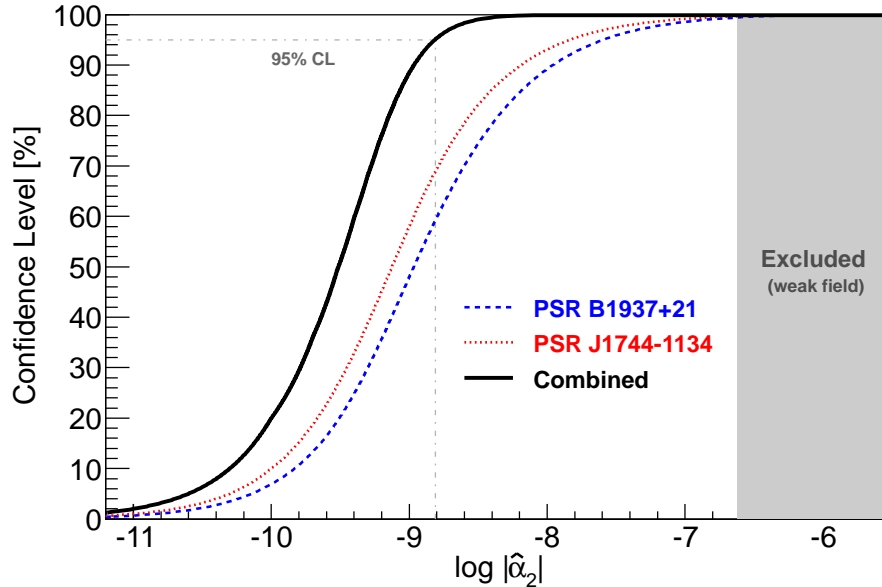


Figure 9. Comparisons of our limits on $|\hat{\alpha}_2|$ with that from the Solar system [47]. The curves show the confidence levels to statistically reject such an $|\hat{\alpha}_2|$ according to the measurements from PSR B1937+21 (blue dashed line), PSR J1744–1134 (red dotted line), and their combination (black solid line). The solar system constraint (2) on the weak-field α_2 [47] is illustrated as the gray region, and the combined limit (15) at 95% confidence level is also indicated.

PSRs B1937+21 and J1744–1134 are independent and that they have approximately the same $\hat{\alpha}_2$ value, we got a combined PDF for $\hat{\alpha}_2$. It is shown in figure 8 as a solid black histogram. The long tail is highly suppressed as one expects. From the combined PDF, we get

$$|\hat{\alpha}_2| < 1.6 \times 10^{-9}, \quad (95\% \text{ CL}) \quad (15)$$

which is significantly better than that of (2) from the Solar system [47], and more than four orders of magnitude better than the limit (6) from LLR [45].

To compare our results with the limit (2) graphically, a logarithmic scale is needed. We plot in figure 9 the confidence levels to exclude a specific $\hat{\alpha}_2$ value versus $\log |\hat{\alpha}_2|$, from PSRs B1937+21 and J1744–1134 and their combination. The limit (2) is plotted as an exclusion region in gray. The improvement of the limit by orders of magnitude is obvious.

5. Discussions

Strictly speaking, the comparison between (2) and (15) is only phenomenological. α_2 and $\hat{\alpha}_2$ probe different aspects of the local Lorentz symmetry of gravity, namely weak fields and strong fields. It was explicitly shown that in the strong fields, one can have a different PPN parameter in the scalar-tensor theories through a mechanism called

“scalarization” similar to the well known phenomenon “phase transition” [14]. As an example, in the scalar-tensor gravity the PPN parameter γ generalizes to

$$\hat{\gamma} \equiv \gamma_{AB} = 1 - \frac{2\alpha_A\alpha_B}{1 + \alpha_A\alpha_B}, \quad (16)$$

for a binary pulsar system, where α_A and α_B are the effective scalar coupling constants of the pulsar and its companion, respectively [13]. The weak-field PPN parameter γ is recovered for $\alpha_A = \alpha_B = \alpha_0$. In GR one has $\hat{\gamma} = \gamma = 1$. Similarly, we may expect that $\hat{\alpha}_2$ deviates from its weak-field PPN correspondent α_2 due to strong-field contributions. The strong-field $\hat{\alpha}_2$ in the Einstein-Æther theory can be found in [19]. In the absence of non-perturbative effects, one can expand $\hat{\alpha}_2$ in the compactness \mathcal{C} of the body [15]. In our case, we would write an expansion like,

$$\hat{\alpha}_2 = \alpha_2 + \mathcal{K}_1\mathcal{C} + \mathcal{K}_2\mathcal{C}^2 + \dots, \quad (17)$$

where \mathcal{K}_i are coefficients characterizing deviations from GR, and $\mathcal{C} \simeq GM/Rc^2$ for a body with mass M and radius R . The compactnesses for the Earth and the Sun are roughly $\mathcal{C}_\oplus \sim 10^{-9}$ and $\mathcal{C}_\odot \sim 10^{-6}$, respectively, which suppress \mathcal{K}_i -related ($i = 1, 2, \dots$) physical effects dramatically. In contrast, neutron stars have $\mathcal{C}_{\text{NS}} \sim 0.2$, which is one of the reasons why pulsars are ideal probes for gravity effects associated with strong gravitational fields. From (17) one can see that, the $\hat{\alpha}_2$ limit from pulsars is $\sim 10^5$ times more sensitive to the \mathcal{K}_1 parameter and $\sim 10^{10}$ times more sensitive to the \mathcal{K}_2 parameter than that of the Solar system test (2). It is even more sensitive compared with the constraint (6) from the ranging experiment of the Sun-Earth-Moon dynamics. This supports the importance of the strong-field $\hat{\alpha}_2$ limit (15).

It is worth mentioning that, when discussing the constraints on strong-field parameters of alternative gravity theories, one should be aware of a potential compactness-dependent nature of these parameters, especially when combining different systems. Our $\hat{\alpha}_2$ test (15) assumes that $\hat{\alpha}_2$ is approximately the same for PSRs B1937+21 and J1744–1134. However, in the presence of phenomena related to some critical mass, like the spontaneous scalarization discovered in the scalar-tensor theory [14], even a small difference in masses does not allow such an assumption (see [16, 22, 1] for constraints on such critical phenomena). Therefore, the comparison between (2), (6), (7) and (15) is only phenomenological. More strictly, they measure different aspects of gravity under different circumstances, such as the gravitational environments of the Sun, the Sun-Earth-Moon orbital dynamics, the pulsar-white dwarf orbital dynamics, and the solitary pulsars.

The main result of the paper (15) is phenomenological in the PPN framework, nevertheless, it is relevant to some alternative gravity theories with local Lorentz invariance violation, like the Hořava-Lifshitz gravity [30, 9], the Einstein-Æther theory [32, 21] and the TeVeS theory [7, 52]. A detailed comparison with these alternative gravity theories has to account for possible strong-field dependencies. Such an analysis is beyond the scope of this paper.

As one can see from figures 8 and 9, the improvement of the combined limit over that from a single pulsar is significant. The combined limit (15) is ten times better

than the one solely obtained from PSR B1937+21 or PSR J1744–1134. This reveals the probabilistic consideration inherent as well as the directional dependence of PFEs. When pulsars located differently and moving with different velocities in different directions are used, the constraint on PFEs is much stronger than solely from one object. It is also demonstrated in [65] for binary pulsars under a similar concept, called “PFE antenna array”. In the $\hat{\alpha}_2$ test, we include two solitary pulsars with highest figure of merit (see below). Through our simulations, we found that by including more pulsars with lower figure of merit, the improvement is not significant. However, two pulsars are the minimum requirement to suppress the long tails discussed earlier.

The figure of merit of the $\hat{\alpha}_2$ test proposed here can be extracted from (12). In general, it depends on the upper limit on the change of pulse width, the spin period, the “absolute” velocity \mathbf{w} , the pulsar’s spin orientation with respect to \mathbf{w} and the line of sight, and also some emission properties encoded in \mathcal{A} . After dropping complicated dependence, one can see that the power of the test is roughly proportional to $[P(dW/dt)^{\text{upper}}]^{-1}$, where $(dW/dt)^{\text{upper}}$ is the upper limit of the change in the pulse width and P is the pulsar spin period. Hence one can see that the solitary pulsars with short spin period and smaller $(dW/dt)^{\text{upper}}$ are more useful in setting a tight constraint of $\hat{\alpha}_2$ ‡. The quantity $(dW/dt)^{\text{upper}}$ can depend on different factors, like the luminosity of the emission, and the pulse width. If we conservatively assume no improvement in the observational technologies, it scales roughly as $T_{\text{obs}}^{-3/2}$, where T_{obs} is the observational time span. Hence finding more pulsars with short spin period, and continuous observations on known MSPs both help in improving the $\hat{\alpha}_2$ limit. In the era of new telescopes, like the Five-hundred-meter Aperture Spherical Telescope (FAST) [46] and the Square Kilometre Array (SKA) [55], with more dedicated technologies, more pulsars are to be found for sure and data with better quality are guaranteed. On the other hand, many stable MSPs are also used in the PTA projects [20, 25, 28] and being observed continuously (like PSRs B1937+21 and J1744–1134), hence the $\hat{\alpha}_2$ test proposed here can be achieved as a byproduct from other science programs, and is expected to improve continuously.

In summary, we proposed to use the non-detection of spin precession of solitary pulsars from pulse profile analysis to constrain the strong-field PPN parameter $\hat{\alpha}_2$. Two solitary pulsars, PSRs B1937+21 and J1744–1134, are used to get a combined limit of $|\hat{\alpha}_2| < 1.6 \times 10^{-9}$ at 95% confidence level (see (15)), which is significantly better than the limit (2) obtained from the Solar system [47]. Moreover, the $\hat{\alpha}_2$ test with solitary pulsars is based on regular observations over the whole time span, excluding for instance a 360° precession between the starting and the end points. In contrast to the Solar limit, our test will continuously improve the limit from finding new pulsars as well as long-term regular observations on known pulsars.

‡ However, in general, all dependencies in (12) contribute; for example, although PSR B1937+21 has a higher $[P(dW/dt)^{\text{upper}}]^{-1}$ compared with PSR J1744–1134, it gets a slightly worse constraint on $\hat{\alpha}_2$ than PSR J1744–1134 because of a significantly larger \mathcal{A} .

Acknowledgments

We are grateful to Kosmas Lazaridis and Oliver Löhmer for helping with observations at the 100-m Effelsberg radio telescope. We thank Ewan Barr, Paulo Freire, Lucas Guillemot, Patrick Lazarus, K.J. Lee, Dominic Schnitzeler, and Joris Verbiest for discussions. We also thank Patrick Lazarus for helping with the reduction of **Asterix** data and Paulo Freire for reading the manuscript. LS is supported by China Scholarship Council (CSC). RNC is a member of the International Max Planck Research School (IMPRS) for Astronomy and Astrophysics at the Universities of Bonn and Cologne. This research has made use of NASA’s Astrophysics Data System.

References

- [1] J. Antoniadis, P. C. C. Freire, N. Wex, *et al.* . A Massive Pulsar in a Compact Relativistic Binary. *Science*, 340:448, 2013.
- [2] D. C. Backer, M. R. Dexter, A. Zepka, *et al.* . A Programmable 36-MHz Digital Filter Bank for Radio Science. *Publications of the Astronomical Society of the Pacific*, 109:61–68, 1997.
- [3] D. C. Backer, S. R. Kulkarni, C. Heiles, A millisecond pulsar. *Nature*, 300:615–618, 1982.
- [4] M. Bailes. Geodetic precession in binary pulsars. *Astronomy and Astrophysics*, 202:109–112, 1988.
- [5] M. Bailes, S. Johnston, J. F. Bell, *et al.* . Discovery of Four Isolated Millisecond Pulsars. *ApJ*, 481:386, 1997.
- [6] Q. G. Bailey and V. A. Kostelecký. Signals for Lorentz violation in post-Newtonian gravity. *Phys. Rev. D*, 74:045001, 2006.
- [7] J. D. Bekenstein. Relativistic gravitation theory for the modified Newtonian dynamics paradigm. *Phys. Rev. D*, 70:083509, 2004. [Erratum: *Phys. Rev. D*, 71:069901, 2005]
- [8] N. D. R. Bhat, J. M. Cordes, F. Camilo, D. J. Nice, and D. R. Lorimer. Multifrequency Observations of Radio Pulse Broadening and Constraints on Interstellar Electron Density Microstructure. *ApJ*, 605:759–783, 2004.
- [9] D. Blas, O. Pujolàs, and S. Sibiryakov. Models of non-relativistic quantum gravity: the good, the bad and the healthy. *Journal of High Energy Physics*, 4:18, 2011.
- [10] J. M. Cordes and T. J. W. Lazio. NE2001.I. A New Model for the Galactic Distribution of Free Electrons and its Fluctuations. arXiv:astro-ph/0207156, 2002.
- [11] J. M. Cordes, I. Wasserman, and M. Blaskiewicz. Polarization of the binary radio pulsar 1913+16 — constraints on geodetic precession. *ApJ*, 349:546–552, 1990.
- [12] T. Damour and G. Esposito-Farèse. Testing local Lorentz invariance of gravity with binary-pulsar data. *Phys. Rev. D*, 46:4128–4132, 1992.
- [13] T. Damour and G. Esposito-Farèse. Tensor-multi-scalar theories of gravitation. *Classical and Quantum Gravity*, 9:2093–2176, 1992.
- [14] T. Damour and G. Esposito-Farèse. Nonperturbative strong-field effects in tensor-scalar theories of gravitation. *Physical Review Letters*, 70:2220–2223, 1993.
- [15] T. Damour and G. Esposito-Farèse. Testing gravity to second post-Newtonian order: A field-theory approach. *Phys. Rev. D*, 53:5541–5578, 1996.
- [16] T. Damour and G. Esposito-Farèse. Tensor-scalar gravity and binary-pulsar experiments. *Phys. Rev. D*, 54:1474–1491, 1996.
- [17] T. Damour and G. Schäfer. New tests of the strong equivalence principle using binary-pulsar data. *Physical Review Letters*, 66:2549–2552, 1991.
- [18] N. D. H. Dass and V. Radhakrishnan. The new binary pulsar and the observation of gravitational spin precession. *Astrophysical Letters*, 16:135–139, 1975.

- [19] B. Z. Foster. Strong field effects on binary systems in Einstein-aether theory. *Phys. Rev. D*, 76:084033, 2007.
- [20] R. D. Ferdman, R. van Haasteren, C. G. Bassa, *et al* . The European Pulsar Timing Array: current efforts and a LEAP toward the future. *Classical and Quantum Gravity*, 27:084014, 2010.
- [21] B. Z. Foster and T. Jacobson. Post-Newtonian parameters and constraints on Einstein-aether theory. *Phys. Rev. D*, 73:064015, 2006.
- [22] P. C. C. Freire, N. Wex, G. Esposito-Farèse, *et al* . The relativistic pulsar-white dwarf binary PSR J1738+0333 - II. The most stringent test of scalar-tensor gravity. *MNRAS*, 423:3328, 2012.
- [23] J. Gil, P. Gronkowski, and W. Rudnicki. Geometry of the emission region of PSR 0950+08. *Astronomy and Astrophysics*, 132:312–316, 1984.
- [24] L. Guillemot, T. J. Johnson, C. Venter, *et al* . Pulsed Gamma Rays from the Original Millisecond and Black Widow Pulsars: A Case for Caustic Radio Emission? *ApJ*, 744:33, 2012.
- [25] R. van Haasteren, Y. Levin, G. H. Janssen, *et al* . Placing limits on the stochastic gravitational-wave background using European Pulsar Timing Array data. *MNRAS*, 414:3117, 2011. [Erratum: *MNRAS*, 425:1597, 2012]
- [26] A. Hewish, S. J. Bell, J. D. H. Pilkington, P. F. Scott, and R. A. Collins. Observation of a Rapidly Pulsating Radio Source. *Nature*, 217:709–713, 1968.
- [27] G. Hinshaw, J. L. Weiland, R. S. Hill, *et al* . Five-Year Wilkinson Microwave Anisotropy Probe Observations: Data Processing, Sky Maps, and Basic Results. *ApJS*, 180:225–245, 2009.
- [28] G. Hobbs, A. Archibald, Z. Arzoumanian, *et al* . The International Pulsar Timing Array project: using pulsars as a gravitational wave detector. *Classical and Quantum Gravity*, 27:084013, 2010.
- [29] G. Hobbs, W. Coles, R. N. Manchester, *et al* . Development of a pulsar-based timescale. *MNRAS*, 427:2780, 2012.
- [30] P. Hořava. Quantum gravity at a Lifshitz point. *Phys. Rev. D*, 79:084008, 2009.
- [31] A. W. Hotan, W. van Straten, and R. N. Manchester. PSRCHIVE and PSRFITS: An Open Approach to Radio Pulsar Data Storage and Analysis. *Publications of the Astronomical Society of Australia*, 21:302–309, 2004.
- [32] T. Jacobson and D. Mattingly. Gravity with a dynamical preferred frame. *Phys. Rev. D*, 64:024028, 2001.
- [33] N. Jarosik, C. L. Bennett, J. Dunkley, *et al* . Seven-year Wilkinson Microwave Anisotropy Probe (WMAP) Observations: Sky Maps, Systematic Errors, and Basic Results. *ApJS*, 192:14, 2011.
- [34] T. J. Johnson. Constraints on the Emission Geometries of Gamma-ray Millisecond Pulsars Observed with the Fermi Large Area Telescope. *PhD thesis*, University of Maryland, 2011. [arXiv:1209.4000]
- [35] K. Kuijken and G. Gilmore. The Mass Distribution in the Galactic Disc – II. Determination of the Surface Mass Density of the Galactic Disc Near the Sun. *MNRAS*, 239:605–649, 1989.
- [36] V. A. Kostelecký. Gravity, Lorentz violation, and the standard model. *Phys. Rev. D*, 69:105009, 2004.
- [37] M. Kramer. Determination of the Geometry of the PSR B1913+16 System by Geodetic Precession. *ApJ*, 509:856–860, 1998.
- [38] M. Kramer, C. Lange, D. R. Lorimer, *et al* . The Characteristics of Millisecond Pulsar Emission. III. From Low to High Frequencies. *ApJ*, 526:957–975, 1999.
- [39] M. Kramer, I. H. Stairs, R. N. Manchester, *et al* . Tests of General Relativity from Timing the Double Pulsar. *Science*, 314:97–102, 2006.
- [40] D. R. Lorimer and M. Kramer. *Handbook of Pulsar Astronomy*. Cambridge University Press, 2005.
- [41] R. N. Manchester, G. Hobbs, M. Bailes, *et al* . The Parkes Pulsar Timing Array Project. *Publications of the Astronomical Society of Australia* , 30:017, 2013.
- [42] R. N. Manchester, G. B. Hobbs, A. Teoh, and M. Hobbs. The Australia Telescope National Facility Pulsar Catalogue. *AJ*, 129:1993–2006, 2005.
- [43] R. N. Manchester, M. Kramer, A. Possenti, *et al* . The Mean Pulse Profile of PSR J0737–3039A.

- ApJ*, 621:L49–L52, 2005.
- [44] R. N. Manchester, M. Kramer, I. H. Stairs, *et al.*. Observations and Modeling of Relativistic Spin Precession in PSR J1141–6545. *ApJ*, 710:1694–1709, 2010.
- [45] J. Müller, J. G. Williams, and S. G. Turyshev. Lunar Laser Ranging Contributions to Relativity and Geodesy. In H. Dittus, C. Lammerzähl, & S. G. Turyshev, editor, *Lasers, Clocks and Drag-Free Control: Exploration of Relativistic Gravity in Space*, volume 349 of *Astrophysics and Space Science Library*, page 457, 2008.
- [46] R. Nan, D. Li, C. Jin, *et al.*. The Five-Hundred Aperture Spherical Radio Telescope (FAST) Project. *International Journal of Modern Physics D*, 20:989–1024, 2011.
- [47] K. Nordtvedt. Probing gravity to the second post-Newtonian order and to one part in 10^7 using the spin axis of the sun. *ApJ*, 320:871–874, 1987.
- [48] K. Nordtvedt, and C. M. Will. Conservation Laws and Preferred Frames in Relativistic Gravity. II. Experimental Evidence to Rule Out Preferred-Frame Theories of Gravity. *ApJ*, 177:775, 1972.
- [49] B. B. P. Perera, M. A. McLaughlin, M. Kramer, *et al.*. The Evolution of PSR J0737–3039B and a Model for Relativistic Spin Precession. *ApJ*, 721:1193–1205, 2010.
- [50] W. H. Press, S. A. Teukolsky, W. T. Vetterling, and B. P. Flannery. *Numerical recipes in FORTRAN*. Cambridge University Press, 1992.
- [51] R. Ramachandran, P. Demorest, D. C. Backer, I. Cognard, and A. Lommen. Interstellar Plasma Weather Effects in Long-Term Multifrequency Timing of Pulsar B1937+21. *ApJ*, 645:303, 2006.
- [52] E. Sagi. Preferred frame parameters in the tensor-vector-scalar theory of gravity and its generalization. *Phys. Rev. D*, 80:044032, 2009.
- [53] D. H. F. M. Schnitzeler. Modelling the Galactic distribution of free electrons. *MNRAS*, 427:664–678, 2012.
- [54] L. Shao and N. Wex. New tests of local Lorentz invariance of gravity with small-eccentricity binary pulsars. *Classical and Quantum Gravity*, 29:215018, 2012.
- [55] R. Smits, M. Kramer, B. Stappers, *et al.*. Pulsar searches and timing with the square kilometre array. *Astronomy and Astrophysics*, 493:1161–1170, 2009.
- [56] M. Soffel, S. Klioner, J. Müller and L. Biskupek. Gravitomagnetism and lunar laser ranging. *Phys. Rev. D*, 78:024033, 2008.
- [57] I. H. Stairs, S. E. Thorsett, and Z. Arzoumanian. Measurement of Gravitational Spin-Orbit Coupling in a Binary-Pulsar System. *Physical Review Letters*, 93:141101, 2004.
- [58] I. H. Stairs, A. J. Faulkner, A. G. Lyne, *et al.*. Discovery of Three Wide-Orbit Binary Pulsars: Implications for Binary Evolution and Equivalence Principles. *ApJ*, 632:1060–1068, 2005.
- [59] J. H. Taylor and J. M. Cordes. Pulsar distances and the galactic distribution of free electrons. *ApJ*, 411:674–684, 1993.
- [60] J. H. Taylor, L. A. Fowler, and P. M. McCulloch. Measurements of general relativistic effects in the binary pulsar PSR 1913+16. *Nature*, 277:437–440, 1979.
- [61] J. H. Taylor and J. M. Weisberg. A new test of general relativity — Gravitational radiation and the binary pulsar PSR 1913+16. *ApJ*, 253:908–920, 1982.
- [62] J. P. W. Verbiest, M. Bailes, W. A. Coles, *et al.*. Timing stability of millisecond pulsars and prospects for gravitational-wave detection. *MNRAS*, 400:951–968, 2009.
- [63] J. P. W. Verbiest, D. R. Lorimer, and M. A. McLaughlin. Lutz–Kelker bias in pulsar parallax measurements. *MNRAS*, 405:564–572, 2010.
- [64] J. M. Weisberg, R. W. Romani, and J. H. Taylor. Evidence for geodetic spin precession in the binary pulsar 1913+16. *ApJ*, 347:1030–1033, 1989.
- [65] N. Wex and M. Kramer. A characteristic observable signature of preferred-frame effects in relativistic binary pulsars. *MNRAS*, 380:455–465, 2007.
- [66] C. M. Will. *Theory and Experiment in Gravitational Physics*. Cambridge University Press, 1993.
- [67] C. M. Will. The Confrontation between General Relativity and Experiment. *Living Rev. Relativity*, 9:3, 2006. [URL (cited on 2013-02-26): <http://www.livingreviews.org/lrr-2006-3>]

- [68] C. M. Will and K. Nordtvedt. Conservation Laws and Preferred Frames in Relativistic Gravity. I. Preferred-Frame Theories and an Extended PPN Formalism. *ApJ*, 177:757, 1972.
- [69] X. P. You, G. Hobbs, W. A. Coles, *et al* . Dispersion measure variations and their effect on precision pulsar timing. *MNRAS*, 378:493, 2007.